

Bifunctional biomorphic SiC ceramics embedded molten salts for ultrafast thermal and solar energy storage

Xu Qiao

Nanjing University of Aeronautics and Astronautics

Xianglei Liu (✉ xliu@nuaa.edu.cn)

Nanjing University of Aeronautics and Astronautics

Qinyang Luo

Nanjing University of Aeronautics and Astronautics

Yanan Song

Nanjing University of Aeronautics and Astronautics

Haolei Wang

Nanjing University of Aeronautics and Astronautics

Meng Chen

Nanjing University of Aeronautics and Astronautics

Yimin Xuan

Nanjing University of Aeronautics and Astronautics

Yongliang Li

School of Chemical Engineering, University of Birmingham

Yulong Ding

School of Chemical Engineering, University of Birmingham

Article

Keywords: Thermal energy storage, solar energy, biomorphic silicon carbide, ceramics, thermal conductivity

Posted Date: January 18th, 2021

DOI: <https://doi.org/10.21203/rs.3.rs-142337/v1>

License:  This work is licensed under a Creative Commons Attribution 4.0 International License.

[Read Full License](#)

Submitted to Nature Communications on 2021/01/06

Bifunctional biomorphic SiC ceramics embedded molten salts for ultrafast thermal and solar energy storage

Qiao Xu¹, Xianglei Liu^{1*}, Qingyang Luo¹, Yanan Song¹, Haolei Wang¹, Meng Chen¹, Yimin Xuan¹, Yongliang Li², Yulong Ding²

1 School of Energy and Power Engineering, Nanjing University of Aeronautics and Astronautics, Nanjing 210016, China

2 Birmingham Centre for Energy Storage, School of Chemical Engineering, University of Birmingham, Birmingham B15 2TT, UK

*Corresponding author e-mail: xliu@nuaa.edu.cn

Abstract

Phase change materials (PCMs) are regarded as one of the most promising candidates for thermal energy storage due to possessing large energy storage densities and maintaining nearly a constant temperature during charging/discharging processes. However, the intrinsically low thermal conductivity of PCMs has become a bottleneck for rapid energy transport and storage. Here, we present a strategy to achieve ultrafast solar and thermal energy storage based on biomorphic SiC skeletons embedded NaCl-KCl molten salts. A record-high thermal conductivity of 116 W/mK is achieved by replicating cellular structure of oak wood, leading to an ultrafast thermal energy storage rate compared with molten salts alone. By further decorating TiN nanoparticles on SiC skeletons, the solar absorptance is enhanced to be as high as 95.63 % via exciting broadband plasmonic resonances. Excellent thermal transport and solar absorption properties enable designed composites to have bifunctional capabilities of harvesting both thermal energy and solar energy very rapidly. This work opens a new route for the design of bifunctional energy storage materials for ultrafast solar and thermal energy storage.

Keywords: Thermal energy storage; solar energy; biomorphic silicon carbide; ceramics; thermal conductivity

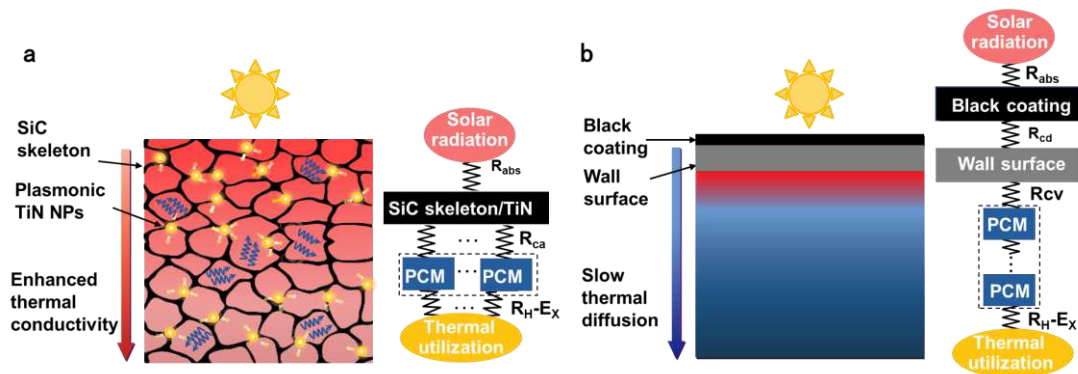
29 **Introduction**

30 Thermal energy storage can bridge the gap between thermal energy supply and
31 consumption, thus playing a vital role in improving overall efficiency and reliability of
32 thermal energy harvesting and utilization systems¹⁻⁴. Among various thermal energy
33 storage materials, phase change materials (PCMs) have been regarded as promising
34 candidates since large amount of heat can be stored or released during phase change
35 processes⁵⁻¹⁵. Besides large energy storage densities, nearly a constant temperature is
36 maintained during thermal energy charging/discharging processes, making output
37 thermal energy have very small temperature variations. However, the intrinsically low
38 thermal conductivity of PCMs (<1 W/mK) makes thermal energy storage process slow⁸,
39 which leads to low thermal energy storage efficiency and low power density. Past
40 efforts in addressing this problem were mainly focused on adding high thermal
41 conductivity fillers into PCMs, such as graphite¹⁶⁻²⁰, graphene²¹, metal or metal oxide
42 particles²²⁻²⁴, metal foams²⁵⁻³¹, carbon nanotubes³², and carbon skeleton³³⁻³⁷. Although
43 effective to some extent^{20, 32, 38-40}, the improvement of thermal conductivity remains
44 limited, so that there is still a long way to realized fast thermal energy transport and
45 storage.

46 Besides being employed for thermal energy storage, PCMs can also store solar
47 energy directly via integrated solar thermal conversion and energy storage, whose
48 schematics is shown in Fig. 1a. For traditional surface-type solar energy storage, solar
49 energy is first absorbed by black coatings and then transferred to bottom PCMs via
50 conduction/convection through black coatings, wall surfaces, and PCMs themselves, as
51 shown in Fig. 1b. Therefore, integrated solar thermal conversion and energy storage
52 techniques can avoid above redundant energy transfer processes, and are more
53 promising for efficient solar energy harvesting. However, most PCMs have poor solar
54 absorption properties, leading to a low solar energy harvesting efficiency. Besides, the
55 low thermal conductivity of PCMs again inhibits fast solar energy harvesting and may
56 cause overheating problems especially near top surfaces. Carbon-based materials, such

57 as carbon nanotubes^{32, 41-44}, graphite⁴⁵⁻⁴⁸, and graphene⁴⁹⁻⁵², have been demonstrated to
 58 improve both solar absorptance and thermal conductivity of PCMs. Nevertheless, these
 59 materials suffer from oxidation problems especially at high temperatures. Therefore,
 60 achieving efficient and fast solar energy storage remains a formidable challenge.

61 Here, we present a strategy to achieve ultrafast thermal and solar energy storage
 62 based on biomorphic SiC skeletons embedded NaCl-KCl molten salts, as shown in Fig.
 63 1b. SiC ceramic is chosen due to its high thermal conductivity, good thermal shock
 64 resistance, and inertness to oxygen or molten salts. Referring to wood's excellent
 65 performance in transporting water and mass, wood-like biomorphic porous SiC
 66 skeletons are fabricated, and the thermal conductivity of PCMs is tremendously
 67 enhanced from 0.84 W/mK to 116 W/mK. Solar absorption can also be enhanced from
 68 22.45 % to 82.00 %. By further decorating TiN nanoparticles (NPs) on porous SiC
 69 skeletons, the solar absorptance is further enhanced to be as high as 95.63 % via exciting
 70 broadband plasmonic resonances. Excellent thermal transport and solar absorption
 71 properties enable designed composites to have bifunctional capabilities of harvesting
 72 both thermal energy and solar energy very rapidly.

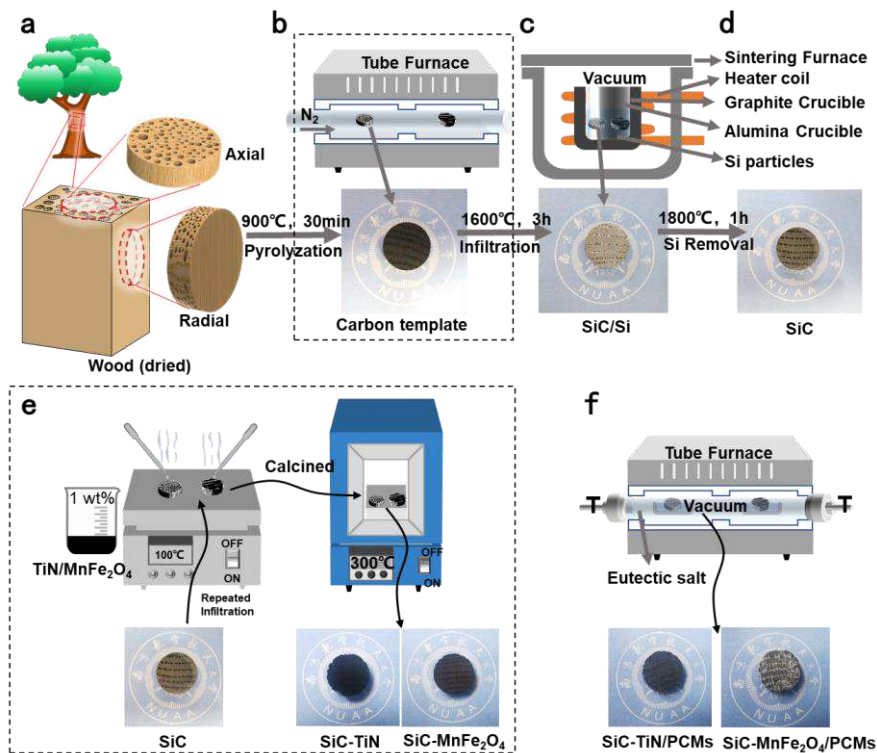


73
 74 Figure 1. Schematic illustration of solar energy storage. **a** Integrated solar thermal conversion and
 75 energy storage. **b** Conventional surface-type.

77 Results

78 **Ultrahigh thermal conductivity enabled by biomorphic SiC foams.** Biomorphic SiC
 79 foams used in this study are fabricated by reactive infiltration of molten silicon into

80 carbonized wood⁵³⁻⁵⁷. Briefly, the wood is first dried for 2~3 days (Fig. 2a), followed
 81 by pyrolyzation and cutting, (Fig. 2b), molten silicon infiltration (Fig. 2c), and then
 82 silicon removal (Fig. 2d). After that, TiN or MnFe₂O₄ NPs are decorated on
 83 biomorphic SiC skeleton surface via dip coating methods, as shown in Fig. 2e. Finally,
 84 eutectic salts are infiltrated into porous SiC skeleton to make biomorphic SiC/TiN-
 85 NaCl-KCl composites (Fig. 2f).

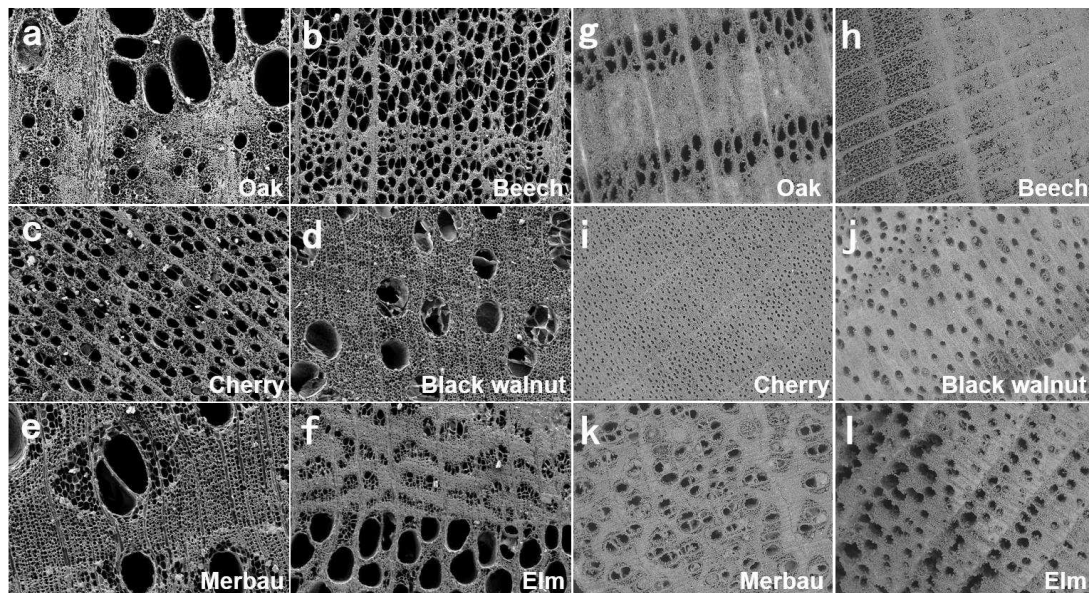


86
 87 Figure 2. Fabrication processes of nanoparticles decorated biomorphic SiC-PCMs composites.

88 Six types of wood are selected as the precursor, the scanning electron microscope
 89 of carbon templates obtained after pyrolysis are shown in Fig. 3a-f, the view is
 90 perpendicular to the direction of growth (axial). As can be clearly seen, carbonized
 91 templates basically reproduce the microstructure of the original wood with channels
 92 parallel to the tree growth direction of the tree, and no cracks or other obvious damages
 93 are observed. Hierarchical pore size distributions are presented for all types of wood,
 94 though different woods show a wide variation in the microstructure and porosities.

95 After molten silicon reactions and removal of the excess Si by sintering at 1800 °C,
 96 biomorphic ceramic can be obtained. Their morphologies are given in Fig. 3g-l, which

97 have an excellent agreement with those of carbonized templates. No excess silicons are
98 observed in the pores for all samples. The empty pores are used to contain PCMs, so
99 that a high thermal energy storage density can be guaranteed.

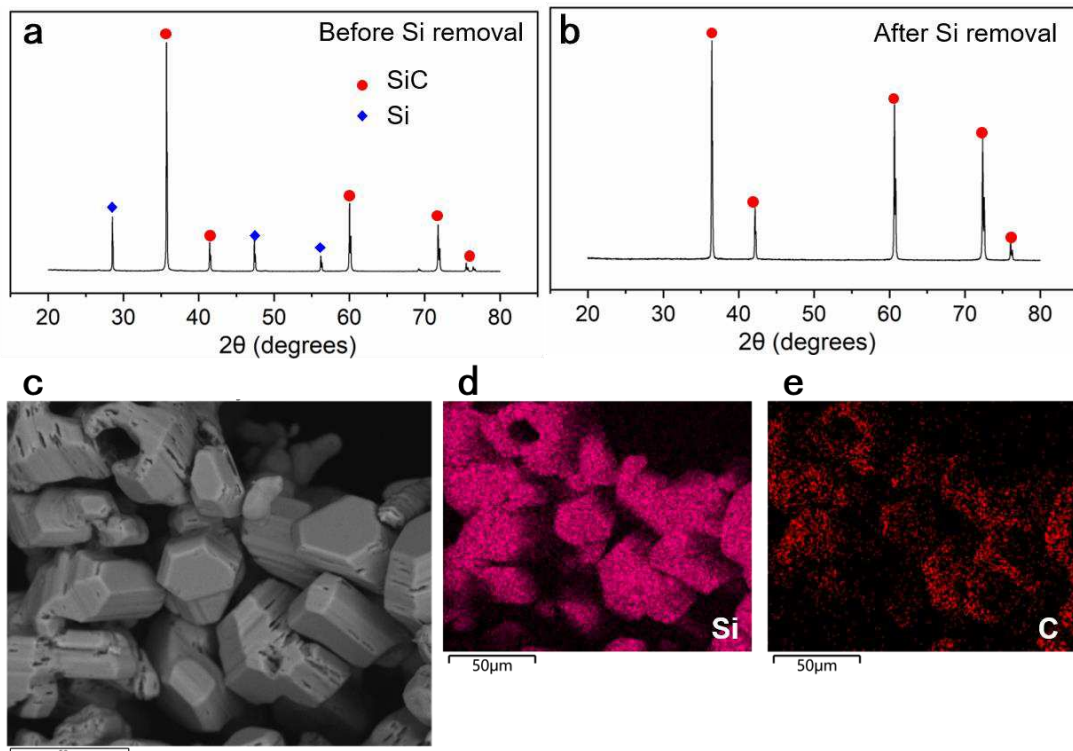


100

101 Figure 3. **a-f** SEM images of carbonized templates (axial sections). **g-l** SEM images of porous
102 biomorphic SiC ceramics (axial sections).

103 To further confirm that all silicon has been removed, X-Ray diffraction patterns
104 of biomorphic SiC before and after silicon removal are shown in Fig. 4a and 4b. Before
105 Si removal, no diffraction peaks of amorphous carbon are observed, indicating that the
106 transformation from carbon template to SiC is completed. Five strong diffraction peaks
107 at $2\theta=36.4^\circ$, 42.18° , and 60.63° , 72.39° , and 76.17° corresponding to cubic type⁵⁸ (β -
108 SiC) occur, confirming the high purity and high crystallinity of SiC. Besides, three
109 diffraction peaks corresponding to Si are found, so the material is Si crystalline. After
110 Si removal, corresponding XRD patterns of silicon disappear, indicating that there is
111 no silicon left. To further confirm it, scanning electron element mapping images (EDS)
112 of the synthesized biomorphic SiC ceramic are given in Fig. 4c-e. Clear boundaries
113 between SiC skeletons and pores are presented, and no silicon elements locating inside
114 pores are observed, further demonstrating that no silicon is left. As also revealed by
115 EDS images, SiC grains have large sizes of 30~50 μm , which helps to reduce gain

116 boundary scattering and improve thermal conductivity. The large crystal size can be
 117 partially attributed to the high temperature heat treatment (1800 °C) used in the
 118 fabrication process to remove the excess silicon, and the grain size may further increase
 119 with increasing temperature. Besides, SiC particles are closely packed with each other,
 120 and there are no impurities around the grain boundary, so that phonon-impurity
 121 scattering is limited. Large grain sizes and absence of impurities make achieving a high
 122 thermal conductivity possible, as will be discussed later.



123
 124 Figure 4. X-ray diffraction patterns of biomorphic SiC ceramics, **a** before and **b** after Si removal. **c**
 125 SEM elemental mapping images of biomorphic SiC ceramics, element of **d** silicon (Si), and **e** Carbon
 126 (C). The ceramic replica was imaged under high vacuum without metal sputtering.

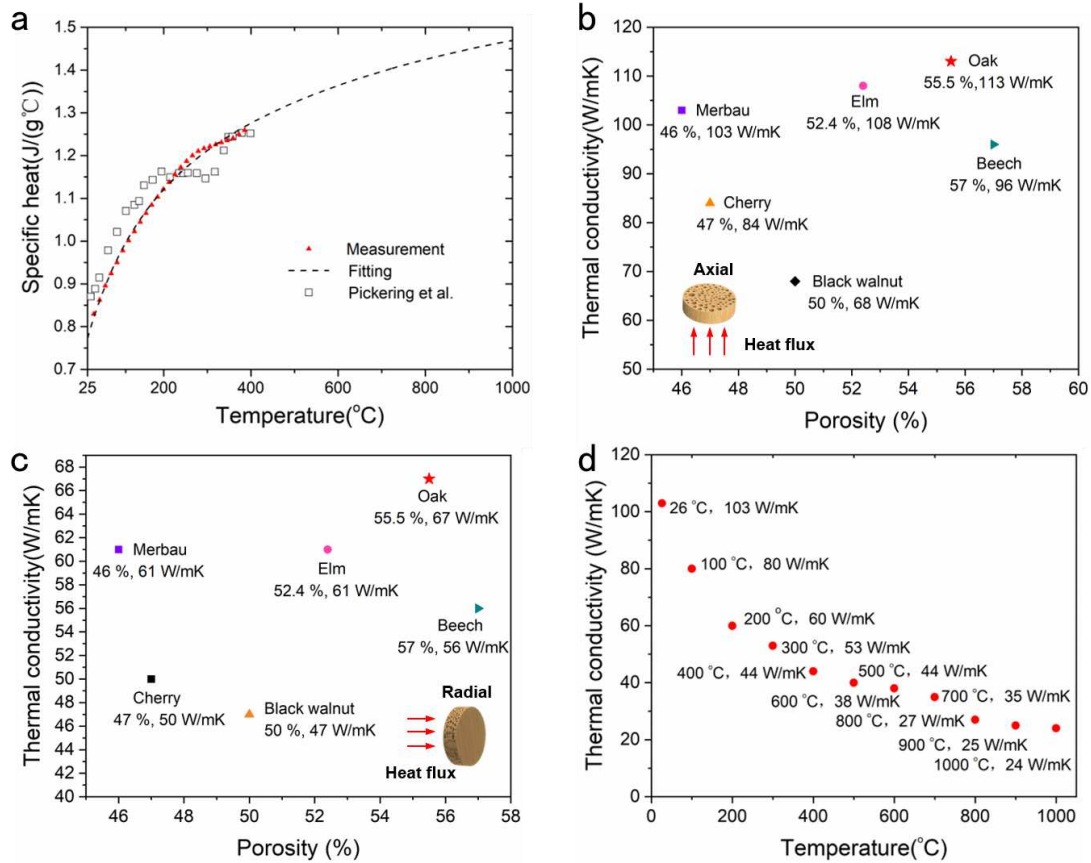
127 The density of the biomorphic SiC porous samples is determined by measuring the
 128 weight and volume of the cylindrical specimens. The porosity of the sample was
 129 calculated by $P(\%) = (1 - \rho_{\text{bioSiC}} / \rho_{\text{SiC}}) \cdot 100\%$, where ρ_{bioSiC} is the density of the porous
 130 biomorphic SiC sample and ρ_{SiC} is the theoretical density of the fully dense SiC⁵⁵ that
 131 is considered to be 3.21 g/cm³. Thermal conductivity (k) was determined according to
 132 the measured thermal diffusivity (α), specific heat (C_p), and density (ρ)⁵⁹:

133
$$k(T) = C_p(T) \cdot \alpha(T) \cdot \rho \quad (1)$$

134 The specific heat capacity of biomorphic SiC is measured from room temperature
135 to 400 °C as given in Fig. 5a, which has a good agreement with literature reports⁶⁰. The
136 specific heat of biomorphic SiC at room temperature is 0.8 J/(g°C), and gradually
137 increases to 1.28 J/(g°C) at 400 °C. Specific heat capacity values over 400 °C can be
138 obtained based on extrapolation fitting. Fig. 5b and 5c present thermal conductivity of
139 different biomorphic SiC samples at room temperature for axial and radial orientations,
140 respectively. The thermal conductivity in the axial direction ranges from 68-113 W/mK,
141 and the highest thermal conductivity obtained is oak-derived SiC ceramic (113 W/mK)
142 at a porosity of 55.5 %. Black walnut-derived SiC ceramic has the lowest conductivity
143 (68 W/mK) although possessing even a lower porosity of 50 %. Therefore, a lower
144 porosity does not necessarily mean a higher thermal conductivity, demonstrating the
145 vital role of microstructures in determining the thermal conductivity. From the
146 comparison between Fig. 5b and 5c, it is easy to tell that the thermal conductivity along
147 the radial direction is much lower compared to the radial case. It is very interesting to
148 note that the thermal conductivity of most biomorphic SiC drops all by around 40 %
149 when switching axial to radial directions. The thermal conductivity of black walnut, on
150 the other hand, drops only about 31 %, although its thermal conductivity is the lowest
151 for both directions.

152 In real applications, biomorphic SiC foams operate at the high melting temperature
153 of PCMs, so that it is necessary to check whether the high thermal conductivity can
154 maintain at high temperatures. Without losing generalities, merbau-derived biomorphic
155 SiC is selected, and its thermal conductivity in the axial orientation is given in Fig. 5d
156 from room temperature to 1000 °C. The thermal conductivity decreases monotonically
157 with increasing temperature. This is expected since phonon-phonon scattering rates
158 increase prominently at high temperatures, leading to a shorter mean free path of
159 phonons, and thus a lower thermal conductivity. Nevertheless, the thermal conductivity
160 is still considerable with a value as high as 24 W/mK when the temperature reaches

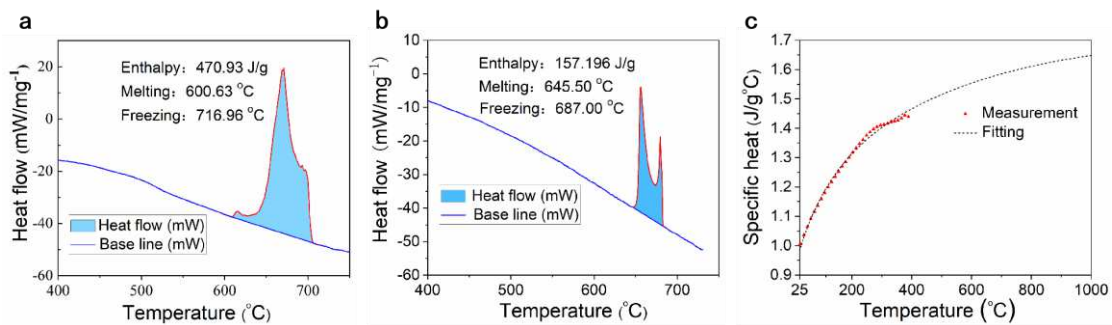
161 1000 °C. Therefore, biomorphic SiC foams are promising candidates to enhance
 162 thermal conductivity of PCMs for a wide temperature range from room temperature to
 163 even 1000 °C.



164
 165 Figure 5. **a** Specific heat of biomorphic SiC at different temperatures. Thermal conductivity versus
 166 porosity at room temperature for both **b** axial and **c** radial orientation for six kinds of wood derived SiC
 167 ceramics. **d** Thermal conductivity of Merbau derived SiC at different temperatures in axial orientations.
 168

169 **Thermal energy storage performances of biomorphic SiC/PCMs composites.** The
 170 energy storage density of the composite material depends largely on the phase change
 171 enthalpy of the PCMs. Here, NaCl and KCl are selected as PCMs due to their high
 172 phase change enthalpies. The differential scanning calorimetry (DSC) curve of the
 173 eutectic PCMs composed of 60 wt% NaCl : 40 wt% KCl is the given in Fig. 6a. A high
 174 fusion enthalpy of 470.93 J/g is obtained, and the starting and ending melting
 175 temperature are 600.63 °C and 716.96 °C, respectively. Such high temperatures are

176 compatible with next-generation solar power plants, whose operating temperature is
 177 expected to be around 700 °C. Oak-derived biomorphic SiC is employed as the skeleton
 178 to package PCMs given its extremely high thermal conductivity. After PCMs are
 179 vacuum-impregnated into porous SiC skeleton, the mass of PCMs is one third of the
 180 total sample. The percentage of the retained PCMs is calculated by
 181 $\eta = (M_{SiC/PCM} - M_{SiC}) / M_{SiC/PCM}$, where η represents the mass fraction of PCMs,
 182 $M_{SiC/PCM}$ denotes the mass of the packaged composites, and M_{SiC} represents the
 183 weight of the SiC. The encapsulation mass ratio is 98 %, so that the energy storage
 184 density of composite material can achieve 157 J/g, which is consistent with the
 185 measured results as given in Fig. 6b. The specific heat of SiC/PCMs composites is given
 186 in Fig. 6c. Substituting this value into Eq. (1), the thermal conductivity of composites
 187 is obtained as 116 W/mK. This is the highest thermal conductivity of non-metal based
 188 phase change composites, to the best of our knowledge.



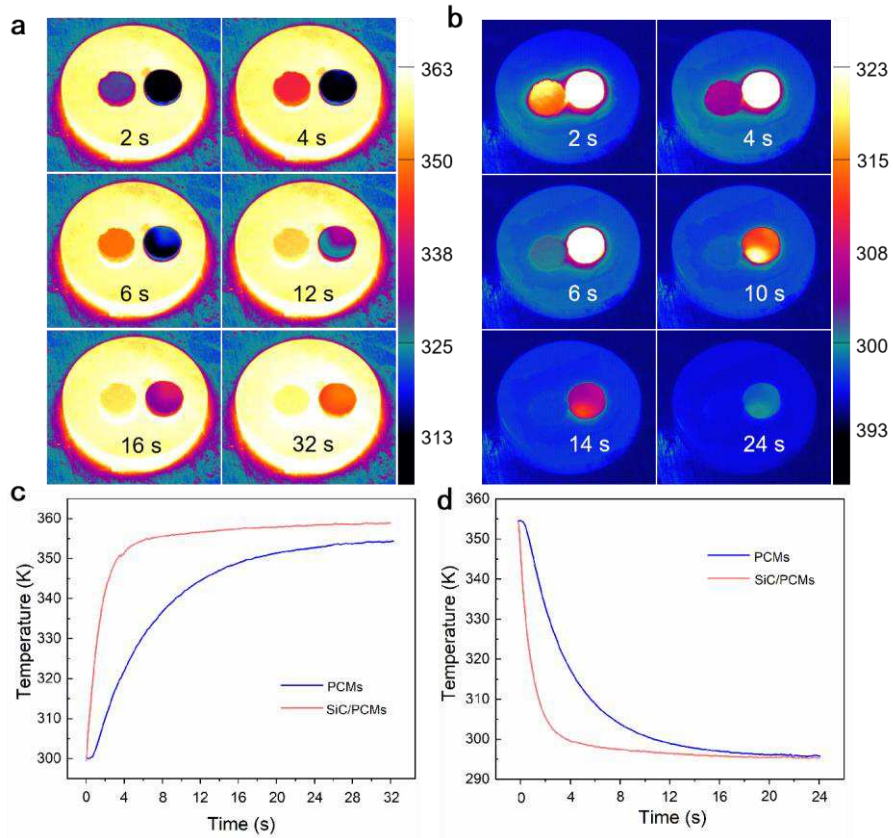
189
 190 Figure 6. DSC curves of **a** PCMs, and **b** SiC/PCMs composites. **c** Specific heat of SiC/PCMs
 191 composites at different temperatures.

192 In order to investigate thermal energy storage performances of SiC/PCMs
 193 composites, surface temperature variations of composites during heating and cooling
 194 processes are recorded by an infrared thermal imager (Fig. 7). During the heating
 195 process, samples are placed on a graphite plate preheated to 90 °C. For the cooling
 196 process, samples are preheated to 90 °C and then placed on a graphite plate at room
 197 temperature immediately. Infrared thermal images of heating and cooling processes are
 198 given in Fig. 7a and 7b, respectively. The left and right sample are SiC /PCMs

199 composites and pure PCMs, respectively. Bottom surfaces of both samples are coated
200 with thermal grease to reduce the contact thermal resistance with graphite plate. Top
201 surfaces are also coated with thermal grease to ensure that two samples have the same
202 emissivity, so that thermal images will be the same if both samples are at the sample
203 temperature. As can be seen clearly in Fig. 7a, the temperature of SiC/PCMs composites
204 rises more quickly compared with pure PCMs. Similar phenomena are also observed
205 for cooling processes, as shown in Fig. 7b. To more intuitively demonstrate the surface
206 changes, Fig. 7c and 7d draw the temperature of surface center of both samples for the
207 heating and cooling process, respectively. The maximum temperature increase rate of
208 composites is 17 K/s, which is 4.2 times as high as that of pure PCMs. Similarly, the
209 maximum temperature drop rate is 26 K/s and 6.85 K/s for composites and PCMs,
210 respectively. Therefore, we can conclude that incorporating biomorphic SiC can
211 dramatically increase the thermal conductivity and thus energy storage and release rate
212 of PCMs, making fast charging/discharging possible.

213

214



215

216

217

218

219

Figure 7. Thermal energy storage properties of SiC/PCMs composites. Infrared thermal images and surface temperature variations for **a** heating and **b** cooling processes. Temperature profiles at the center of sample surfaces for **c** heating and **d** cooling processes.

220

Solar energy storage performances of biomorphic SiC-TiN/PCMs composites.

221

Biomorphic SiC/PCMs have been demonstrated to possess excellent thermal energy

222

storage performances. If we want proposed samples to operate well when the energy

223

source is not heat but solar energy directly, samples should, first of all, possess a high

224

solar absorptance. As shown in Fig. 8a, pure PCMs have a low solar absorptance $A(\lambda)$

225

especially in the visible range where solar irradiation $S(\lambda)$ is high. Incorporating

226

biomorphic SiC can prominently enhance the solar absorptance for almost all

227

wavelengths from 200 to 2000 nm. As a result, the average solar absorptance, calculated

228

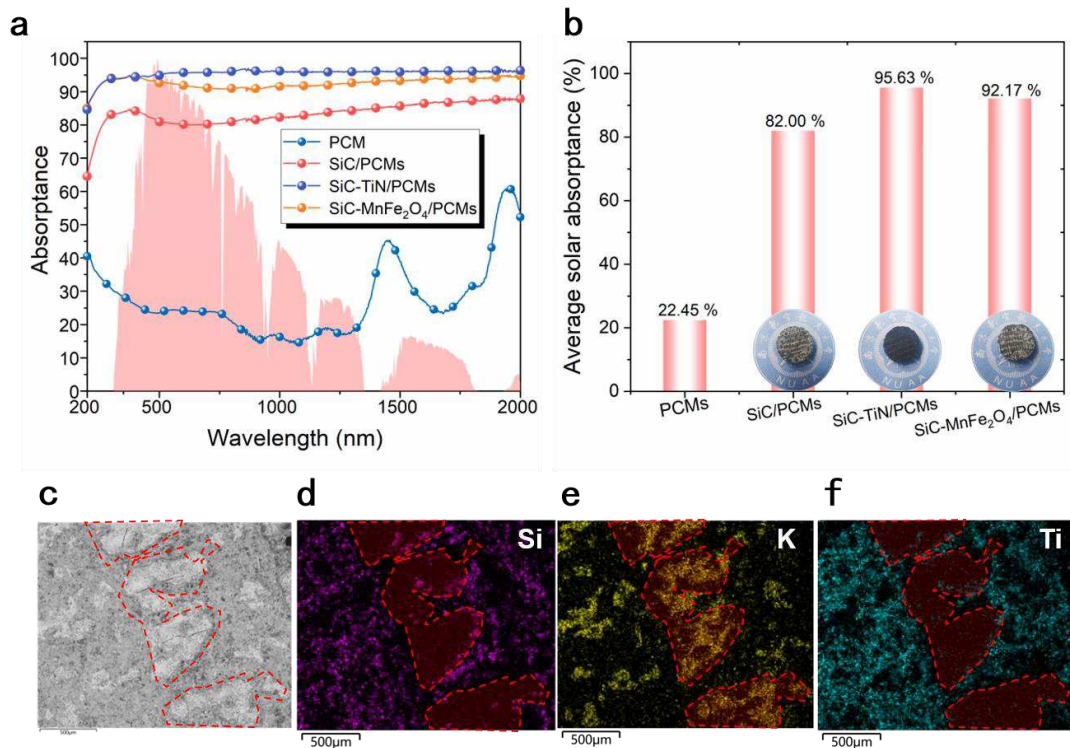
via $A = \frac{\int_{200}^{2000} A(\lambda)S(\lambda)d\lambda}{\int_{200}^{2000} S(\lambda)d\lambda}$, is improved from 22.45% to 82.00% as can

229

be seen clearly in Fig. 8b. More intuitively, the color changes from white to gray.

230 Nevertheless, there is still much room for further improving capability of capturing
231 solar energy. Ceramic TiN nanoparticles have been known to trap light well by exciting
232 surface plasmon resonances in a broad band⁶¹⁻⁶³. Subsequently, dip coating methods are
233 employed to deposit TiN nanoparticles on biomorphic SiC surfaces in order to further
234 elevate solar absorptance. Black MnFe₂O₄ nanoparticles are also investigated. Briefly,
235 TiN or MnFe₂O₄ nanoparticles are mixed with deionized water at a ratio of 1:100 (wt %),
236 the biomorphic SiC ceramic is dipped in the mixture of TiN-DI or MnFe₂O₄-DI,
237 respectively, and dried at 373 K, followed by sintering processes at 573 K for 2 hours.
238 The weight increase of samples after being decorated with TiN or MnFe₂O₄ are both
239 approximately 0.01 g, meaning that the percentage of nanoparticles to the whole sample
240 is only about 1.2 wt%. Nevertheless, the spectral absorptance is greatly enhanced for
241 the whole spectrum. As a result, the average solar absorptance achieves 92.17 % and
242 95.29 % by decorating MnFe₂O₄ and TiN nanoparticles, respectively.

243 EDS images of SiC-TiN/PCMs composites are given in Fig. 8c~8f. As shown in
244 Fig. 8c, the shaded region represents PCMs, whose color is white. Elements of silicon
245 (Si) and potassium (K) represent distributions of biomorphic SiC skeletons and PCMs,
246 respectively, as shown in Fig. 8d and 8e. Skeletons and PCMs are complementary to
247 each other, and most pores are filled with PCMs. This is in a good agreement with the
248 measured loading ratio of PCMs, which is as high as 98%. Distributions of Ti element
249 are very similar to those of Si, as shown in Fig. 8f. This means that TiN nanoparticles
250 indeed are decorated on SiC surfaces rather than inside pores, which further helping to
251 achieve a high loading ratio of PCMs and thus a high energy storage density.



252

253

254

255

f titanium (Ti).

256

257

258

259

260

261

262

263

264

265

266

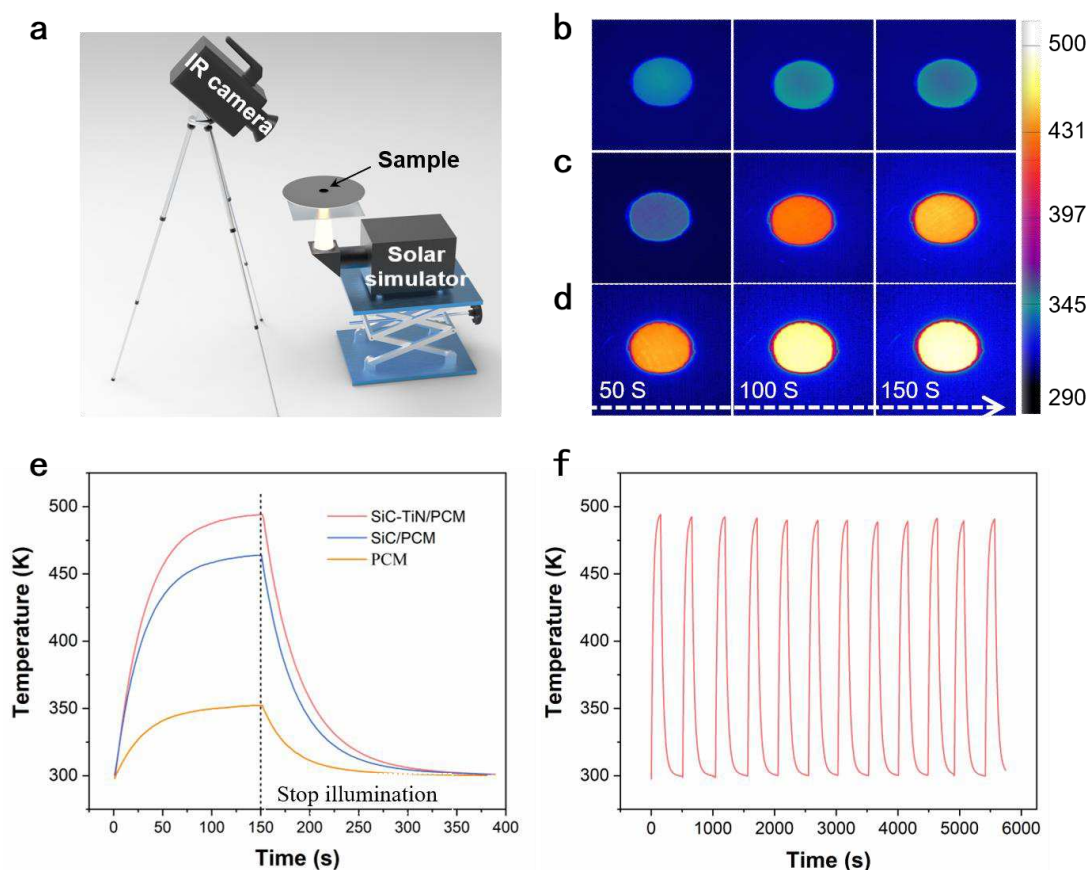
267

268

Figure 8. **a** Spectral and **b** average solar absorptance of SiC/PCMs, SiC-TiN/PCMs, and SiC-MnFe₂O₄/PCMs. **c** EDS images of the SiC-TiN/PCMs, elements of **d** silicon (Si), **e** potassium (K), and **f** titanium (Ti).

Since both the thermal conductivity and solar absorptance have been enhanced tremendously, now it is time to check the solar energy storage performances of proposed samples. Concentrated solar radiation with a power density of 5 W/cm² generated by a solar simulator was used to illuminate the sample from the bottom, as demonstrated in Fig. 9a. Time-sequential IR images of PCMs, SiC/PCMs, and SiC-TiN/PCMs are displayed in Fig. 9b, 9c, and 9d, respectively. For pure PCMs, the temperature increases very slowly under irradiation of light. Main reasons can be attributed to the low thermal conductivity and poor solar absorptance. For SiC/PCMs and SiC-TiN/PCMs, temperature quickly rise to high values even at the beginning 50s due to their high thermal conductivities. The temperature of SiC-TiN/PCMs is higher due to better solar absorption properties enabled by TiN nanoparticles. Fig. 9c draws temperature values of three kinds of thermal storage materials during solar-driven heating and natural cooling processes. Indeed, SiC-TiN/PCMs have the highest energy storage rate under

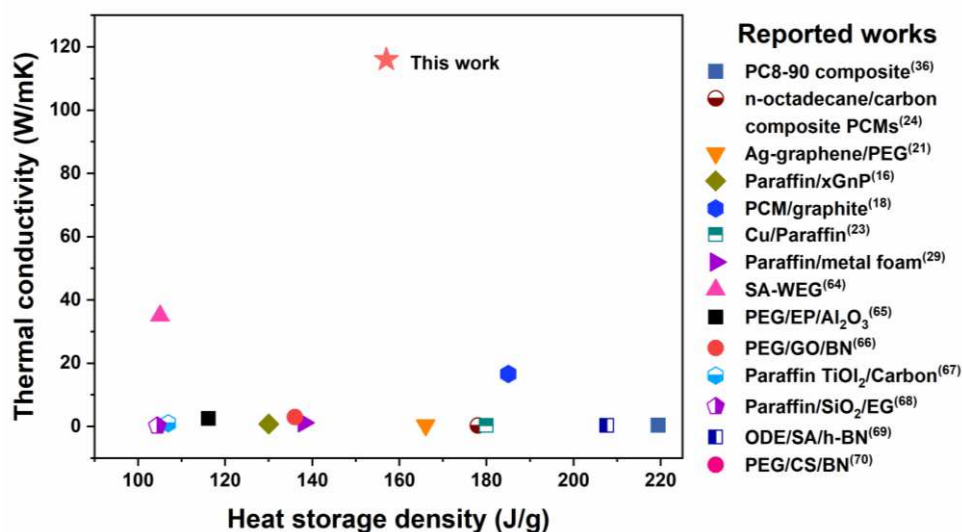
269 the light illumination due to the synthetic effects of high thermal conductivity and high
 270 solar absorptance. Fig. 9f gives the temperature change of SiC-TiN/PCMs composites
 271 during 12 consecutive heating and cooling cycles. As can be seen clearly, the
 272 temperature profile exhibits excellent cycle stability without no obvious deteriorations
 273 of the maximum temperature. Therefore, SiC-TiN/PCMs composites are able to achieve
 274 fast and stable solar energy storage performances.



275
 276 Figure 9. Solar energy storage performances. **a** Schematic experimental setup. IR images of **b** pure
 277 PCMs, **c** SiC/PCMs, and **d** SiC-TiN/PCMs. **e** Temperature profiles in the center of sample surfaces. **f**
 278 Temperature profiles during repeated heating and cooling processes.

279 Figure. 10 shows a comparison of the thermal conductivity and the energy density
 280 of PCMs composites from the latest reports with our proposals. Some materials
 281 possessing high energy storage density, like PC8-90 composite, usually have a low
 282 thermal conductivity. One the other hand, after enhancing the thermal conductivity by
 283 adding more fillers, the energy storage density will decrease tremendously. High

284 thermal conductivity and high energy storage density are usually not compatible, but
 285 are achieved simultaneously by biomorphic SiC-TiN/PCMs composites. It can be seen
 286 clearly, the thermal conductivity of biomorphic SiC-TiN/PCMs composites (116 W/mK)
 287 is much larger than currently reported values. The energy storage density of 157J/g is
 288 also considerable. Besides storing heat, proposed composites can be also used to store
 289 solar energy directly with both excellent solar absorption properties and fast solar
 290 energy storage rates.



291
 292 Figure. 10. A comparison of the thermal conductivity and heat storage density of phase
 293 change composites from the latest reports
 294

295 **Methods**

296 **Preparation processes of biologic ceramics.** Porous biomorphic SiC skeletons are
 297 fabricated by infiltration of liquid silicon into porous carbon templates obtained from
 298 pyrolysis of natural wood. Six wood precursors with different porosities are used: oak,
 299 merbau, beech, elm, black walnut, and maple. The manufacturing process consists of
 300 three steps. First, the wood specimens are cut, dried for 2 to 3 days at 70 °C, and
 301 pyrolyzed in an inert atmosphere, resulting in porous carbon templates. During
 302 pyrolysis, a slow heating rate of 0.5 °C/min is used up to complete decomposition of
 303 the polyaromatic wood polymers (cellulose, hemicellulose, and lignin) at 500 °C. Then

304 a higher heating rate of 1°C/min up to 900 °C is used followed by a hold time of 30 min.
305 By using slow heating rates during pyrolysis, crack-free carbon monoliths could be
306 obtained. The porous carbon templates obtained are machined to small disks with 12.7
307 mm in diameter and 3 mm in thickness with their axes parallel (axial - ||) or
308 perpendicular (radial - ⊥) to the tree growth directions as shown in Fig. 2b.

309 Second, the carbon templates are infiltrated with Si particles (20-100 μm,
310 Aladdin 99.99 % purity; shanghai, China) in vacuum at 1600 °C for 3 h. The quantities
311 of Si particles are above the stoichiometric ratio to carbon to ensure that carbon
312 templates are completely converted to SiC ceramics, and the time used is enough to
313 achieve complete reaction and stable microstructures. After this process, the resulting
314 material is SiC/Si composites that mimics the microstructure of the original wood
315 precursor, and the channels of the sample completely or partially filled with residual
316 silicon (Fig. 2c).

317 Third, the biomorphic SiC /Si composites are heated up to 1800 °C in vacuum to
318 remove the excess Si, the heating rate is 15 °C/min. In the process of removing excess
319 Si, the way to determine whether the Si has been removed completely is not the
320 sintering time but the change in the vacuum degree. As the temperature rises, the silicon
321 vapor escapes and the vacuum degree gradually increases. When most of the silicon is
322 removed, the vacuum degree gradually decreases. However, there is still silicon left in
323 the pores, one more hour is need to remove the silicon completely. In this process, each
324 sample needs to be placed at intervals, stacking is harmful to sample sintering. Besides,
325 note that the wood contains trace elements, and the decomposition of SiC occurs when
326 it is held for a long time at high temperature. The final material obtained after this
327 process is biomorphic SiC that consists of a highly porous SiC skeleton that reproduces
328 the cellular morphology of natural wood (Fig. 2d).

329 In order to enhance the spectral absorbance of SiC ceramics, titanium nitride and
330 manganese ferrite (MnFe₂O₄) are employed to be loaded on the SiC skeleton. Titanium
331 nitride (Aladdin 99.9 %; shanghai, China) with particles size of 20 nm or MnFe₂O₄

332 (prepared by using sol-gel method) are mixed with deionized water at a ratio of 1:100
333 (wt%). The wood-derived SiC ceramics are dipped in the mixture of TiN-DI or
334 MnFe₂O₄-DI, respectively, and dried at 373 K. This process is repeated several times
335 until the green SiC ceramic turned black. And then the SiC samples that loaded with
336 TiN or MnFe₂O₄ are sintered at 573 K in a Muffle furnace (Fig. 2e).

337

338 **Preparation of phase change material and SiC/PCMs composites.** Sodium chloride
339 and potassium chloride (60:40 wt%) (Aladdin 99.5 % AR purity; shanghai, China) are
340 mixed thoroughly in a ball mill at a speed of 300 r/min for 3 h. Then the mixed salt is
341 dried in nitrogen atmosphere at 423 K for 24 h and then dried at 623 k for 2 h to get the
342 PCMs.

343 Biomorphic SiC that decorated with nanoparticles and the solid chloride mixture
344 are placed in the container, and heated up to 670 °C in vacuum for 4 h to ensure that
345 PCMs are totally melted and infiltrated into the cells, and then cooled down until PCMs
346 are solidified, as shown in Fig. 2 (f).

347

348 **Characterization.** A scanning electron microscope (SEM, Hitachi-FE-SEM-S-4800)
349 equipped with secondary electron (SE) and backscattered electron (BSE) detectors is
350 used to observe the microstructure of biomorphic SiC and SiC-TiN/PCMs, so
351 compositional contrast between the phases could be obtained. Phase analysis are
352 performed by X-ray diffraction (XRD), analyses are carried out in samples before and
353 after the process of Si removal.

354 The enthalpy value of composite PCMs and the specific heat capacity (C_p) of the
355 SiC porous sample are investigated using a differential scanning calorimeter (DSC,
356 MET-TLER TOLEDO-DSC-1) at 10 °C/min with nitrogen gas flow of 50 mL/min. Due
357 to the microstructural independence of C_p and the same experimental process of all the
358 biomorphic SiC samples, only one type of biomorphic SiC is tested and the C_p of SiC
359 skeleton derived from different wood precursor is assumed to be equal.

360 The thermal diffusivity (α) of the biomorphic SiC and the composite sample are
361 measured by the laser flash method (Linseis LFA500), which is a widely used technique
362 to determine the diffusivity of materials. A flash of a laser or a flash xenon lamp is
363 uniformly imparted onto one surface of the cylinder sample. The infrared detector
364 continuously monitors the temperature rise on the opposite side. The temperature versus
365 with time on the opposite of the sample is recorded. The thermal diffusivity value is
366 calculated according to the equation: $\alpha = \omega L^2 / \pi t_{1/2}$, where α is the thermal diffusivity in
367 cm^2/s , L is the sample thickness, ω is a constant determined by Clark and Taylor
368 approximation and $t_{1/2}$ is the time that the other side of the sample to reach half of its
369 maximum temperature.

370 Measurements of the thermal diffusivity in both axial and radial orientations are
371 performed on disk-shaped samples with 12.7 mm in diameter and 3 mm in thickness.
372 The diffusivity of the samples in the temperature range of 100-1000°C at approximately
373 100°C intervals was measured in an argon atmosphere. A xenon flash was shot at each
374 samples at least three times, and the data is analyzed by using the software, which
375 including Clark and Taylor approximations. The diffusivity of each sample is obtained
376 by averaging the results of the subsequent rounds after the result of the first time is
377 discarded. At each temperature, three samples from the same wood precursor type and
378 orientation were tested, the results are an average of the three samples. Density was
379 assumed to be constant throughout the high-temperature testing.

380

381 **Discussion**

382 In summary, we successfully achieved ultrafast both solar and thermal energy storage
383 based on biomorphic SiC skeletons embedded NaCl-KCl molten salts. A record-high
384 thermal conductivity of 116W/mK is realized by replicating cellular structure of oak
385 wood, relieving the low thermal conductivity bottleneck of PCMs. After further
386 decorating TiN nanoparticles on SiC skeletons, excellent solar energy capture capability
387 with 95% of solar absorptance is achieved via exciting broadband plasmonic resonances.

388 Excellent thermal transport and solar absorption properties enable designed composites
389 to have bifunctional capabilities of harvesting both thermal energy and solar energy
390 very rapidly. We believe this work opens a new avenue for the design of ceramics based
391 phase change composites to harvest solar and thermal energy simultaneously with a fast
392 rate and high efficiency.

393

394 **Data availability.** The data that support the findings of this study are available from
395 the corresponding author on request upon reasonable request.

396

397 **References**

- 398 1. Steven, Chu, Arun, Nature MJ. Opportunities and challenges for a sustainable
399 energy future. *Nature* **488**, 294-303 (2012).
- 400 2. Lewis NS. Toward Cost-Effective Solar Energy Use. *Science* **315**, 798-801
401 (2007).
- 402 3. Ruiting, *et al.* Reversible temperature regulation of electrical and thermal
403 conductivity using liquid-solid phase transitions. *Nature Communications* **2**, 1-
404 6 (2011).
- 405 4. Tokoro H, *et al.* External stimulation-controllable heat-storage ceramics. *Nature*
406 *Communications* **6**, 1-8 (2015).
- 407 5. Kenisarin M, Mahkamov K. Solar energy storage using phase change materials.
408 *Renewable and sustainable energy reviews* **11**, 1913-1965 (2007).
- 409 6. Kenisarin MM. High-temperature phase change materials for thermal energy
410 storage. *Renewable and Sustainable energy reviews* **14**, 955-970 (2010).
- 411 7. Mondal S. Phase change materials for smart textiles—An overview. *Applied*
412 *thermal engineering* **28**, 1536-1550 (2008).
- 413 8. Pielichowska K, Pielichowski K. Phase change materials for thermal energy
414 storage. *Progress in materials science* **65**, 67-123 (2014).
- 415 9. Sharma A, Tyagi VV, Chen C, Buddhi D. Review on thermal energy storage
416 with phase change materials and applications. *Renewable and Sustainable*
417 *energy reviews* **13**, 318-345 (2009).
- 418 10. Vu MC, Thieu NAT, Choi WK, Islam MA, Kim S-R. Ultralight covalently
419 interconnected silicon carbide aerofoam for high performance thermally
420 conductive epoxy composites. *Composites Part A: Applied Science and*
421 *Manufacturing* **138**, 106028 (2020).
- 422 11. Wuttig M, Yamada N. Phase-change materials for rewriteable data storage.
423 *Nature materials* **6**, 824-832 (2007).
- 424 12. Zalba B, Marin JM, Cabeza LF, Mehling H. Review on thermal energy storage
425 with phase change: materials, heat transfer analysis and applications. *Applied*
426 *thermal engineering* **23**, 251-283 (2003).
- 427 13. Lencer D, Salinga M, Grabowski B, Hickel T, Neugebauer J, Wuttig M. A map
428 for phase-change materials. *Nature materials* **7**, 972-977 (2008).
- 429 14. A AS, B VVT, A CRC, B DB. Review on thermal energy storage with phase
430 change materials and applications. *Renewable & Sustainable Energy Reviews*
431 **13**, 318-345 (2009).
- 432 15. Han GGD, Li H, Grossman JCJNC. Optically-controlled long-term storage and
433 release of thermal energy in phase-change materials. *Nature Communications* **8**,
434 1-10 (2017).
- 435 16. Kim S, Drzal LT. High latent heat storage and high thermal conductive phase
436 change materials using exfoliated graphite nanoplatelets. *Solar Energy*
437 *Materials and Solar Cells* **93**, 136-142 (2009).

- 438 17. Ling Z, Chen J, Xu T, Fang X, Gao X, Zhang Z. Thermal conductivity of an
439 organic phase change material/expanded graphite composite across the phase
440 change temperature range and a novel thermal conductivity model. *Energy*
441 *Conversion and Management* **102**, 202-208 (2015).
- 442 18. Mills A, Farid M, Selman J, Al-Hallaj S. Thermal conductivity enhancement of
443 phase change materials using a graphite matrix. *Applied Thermal Engineering*
444 **26**, 1652-1661 (2006).
- 445 19. Ge Z, Ye F, Ding Y. Composite Materials for Thermal Energy Storage:
446 Enhancing Performance through Microstructures. *Chemsuschem* **7**, 1318 (2014).
- 447 20. Shi J-N, *et al.* Improving the thermal conductivity and shape-stabilization of
448 phase change materials using nanographite additives. *Carbon* **51**, 365-372
449 (2013).
- 450 21. Zhang Y, *et al.* Ag-graphene/PEG composite phase change materials for
451 enhancing solar-thermal energy conversion and storage capacity. *Applied*
452 *Energy* **237**, 83-90 (2019).
- 453 22. Wang Z, *et al.* Rapid Charging of Thermal Energy Storage Materials through
454 Plasmonic Heating. *Scientific Reports* **4**, 6246 (2014).
- 455 23. Wu S, Zhu D, Zhang X, Huang J. Preparation and Melting/Freezing
456 Characteristics of Cu/Paraffin Nanofluid as Phase-Change Material (PCM).
457 *Energy & Fuels* **24**, 1894-1898 (2010).
- 458 24. Teng TP, Yu CC. Characteristics of phase-change materials containing oxide
459 nano-additives for thermal storage. *Nanoscale Research Letters* **7**, 611-611
460 (2012).
- 461 25. Chen J, Yang D, Jiang J, Ma A, Song D. Research progress of phase change
462 materials (PCMs) embedded with metal foam (a review). *Procedia Materials*
463 *Science* **4**, 389-394 (2014).
- 464 26. Chen Z, Gao D, Shi J. Experimental and numerical study on melting of phase
465 change materials in metal foams at pore scale. *International journal of heat and*
466 *mass transfer* **72**, 646-655 (2014).
- 467 27. Li W, Qu Z, He Y, Tao Y. Experimental study of a passive thermal management
468 system for high-powered lithium ion batteries using porous metal foam
469 saturated with phase change materials. *Journal of power sources* **255**, 9-15
470 (2014).
- 471 28. Tian Y, Zhao C-Y. A numerical investigation of heat transfer in phase change
472 materials (PCMs) embedded in porous metals. *Energy* **36**, 5539-5546 (2011).
- 473 29. Xiao X, Zhang P, Li M. Preparation and thermal characterization of
474 paraffin/metal foam composite phase change material. *Applied Energy* **112**,
475 1357-1366 (2013).
- 476 30. Zhao C, Lu W, Tian Y. Heat transfer enhancement for thermal energy storage
477 using metal foams embedded within phase change materials (PCMs). *Solar*
478 *energy* **84**, 1402-1412 (2010).

- 479 31. Zhou D, Zhao C. Experimental investigations on heat transfer in phase change
480 materials (PCMs) embedded in porous materials. *Applied Thermal Engineering*
481 **31**, 970-977 (2011).
- 482 32. Wang Y, Tang B, Zhang S. Single - Walled Carbon Nanotube/Phase Change
483 Material Composites: Sunlight - Driven, Reversible, Form - Stable Phase
484 Transitions for Solar Thermal Energy Storage. *Advanced Functional Materials*
485 **23**, 4354-4360 (2013).
- 486 33. Wang C, Feng L, Li W, Zheng J, Tian W, Li X. Shape-stabilized phase change
487 materials based on polyethylene glycol/porous carbon composite: the influence
488 of the pore structure of the carbon materials. *Solar Energy Materials and Solar*
489 *Cells* **105**, 21-26 (2012).
- 490 34. Yang Z, Deng Y, Li J. Preparation of porous carbonized woods impregnated
491 with lauric acid as shape-stable composite phase change materials. *Applied*
492 *Thermal Engineering* **150**, 967-976 (2019).
- 493 35. Zhao Y, Min X, Huang Z, Liu Yg, Wu X, Fang M. Honeycomb-like structured
494 biological porous carbon encapsulating PEG: A shape-stable phase change
495 material with enhanced thermal conductivity for thermal energy storage. *Energy*
496 *and Buildings* **158**, 1049-1062 (2018).
- 497 36. Atinafu DG, Dong W, Wang C, Wang G. Synthesis of porous carbon from cotton
498 using an Mg (OH) 2 template for form-stabilized phase change materials with
499 high encapsulation capacity, transition enthalpy and reliability. *Journal of*
500 *Materials Chemistry A* **6**, 8969-8977 (2018).
- 501 37. Ji R, *et al.* Enhanced thermal performance of form-stable composite phase-
502 change materials supported by novel porous carbon spheres for thermal energy
503 storage. *Journal of Energy Storage* **27**, 101134 (2020).
- 504 38. Li Y, Samad YA, Polychronopoulou K, Alhassan SM, Liao K. From biomass to
505 high performance solar-thermal and electric-thermal energy conversion and
506 storage materials. *Journal of Materials Chemistry A* **2**, 7759-7765 (2014).
- 507 39. Huang X, Xia W, Zou R. Nanoconfinement of phase change materials within
508 Carbon Aerogels: Phase Transition Behaviours and Photo-to-Thermal Energy
509 Storage. *Journal of Materials Chemistry A* **2**, 19963-19968 (2014).
- 510 40. Li Y, Mai YW, Ye L. Sisal fibre and its composites: a review of recent
511 developments. *Composites Science & Technology* **60**, 2037-2055 (2000).
- 512 41. Shaikh S, Lafdi K, Hallinan KJJoAP. Carbon nanoadditives to enhance latent
513 energy storage of phase change materials. *Journal of applied physics* **103**,
514 094302 (2008).
- 515 42. Xu B, Li ZJE. Paraffin/diatomite/multi-wall carbon nanotubes composite phase
516 change material tailor-made for thermal energy storage cement-based
517 composites. *Energy* **72**, 371-380 (2014).
- 518 43. Lane GAJSEM, Cells S. Phase change materials for energy storage nucleation
519 to prevent supercooling. *Solar Energy Materials and Solar Cells* **27**, 135-160
520 (1992).

- 521 44. Kolpak AM, Grossman JCJNL. Azobenzene-Functionalized Carbon Nanotubes
522 As High-Energy Density Solar Thermal Fuels. *Nano Letters* **11**, 3156-3162
523 (2011).
- 524 45. Sanusi O, Warzoha R, Fleischer ASJIJoH, Transfer M. Energy storage and
525 solidification of paraffin phase change material embedded with graphite
526 nanofibers. *International journal of heat and mass transfer* **54**, 4429-4436
527 (2011).
- 528 46. Pincemin S, Olives R, Py X, Christ MJSEM, Cells S. Highly conductive
529 composites made of phase change materials and graphite for thermal storage.
530 *solar Energy Materials and Solar Cells* **92**, 603-613 (2008).
- 531 47. Py X, Olives R, Mauran SJIJoH, Transfer M. Paraffin/porous-graphite-matrix
532 composite as a high and constant power thermal storage material. *International*
533 *journal of heat and mass transfer* **44**, 2727-2737 (2001).
- 534 48. Sar A, Karaipekli AJSEM, Cells S. Preparation, thermal properties and thermal
535 reliability of palmitic acid/expanded graphite composite as form-stable PCM
536 for thermal energy storage. *solar Energy Materials and Solar Cells* **93**, 571-576
537 (2009).
- 538 49. Cottrill AL, *et al.* Ultra-high thermal effusivity materials for resonant ambient
539 thermal energy harvesting. *nature Communications* **9**, 664 (2018).
- 540 50. Mo R, Rooney D, Sun K, Yang HYJNC. 3D nitrogen-doped graphene foam with
541 encapsulated germanium/nitrogen-doped graphene yolk-shell nanoarchitecture
542 for high-performance flexible Li-ion battery. *nature Communications* **8**, 13949
543 (2017).
- 544 51. Liang W, *et al.* Graphene–nickel/n-carboxylic acids composites as form-stable
545 phase change materials for thermal energy storage. *Solar Energy Materials and*
546 *Solar Cells* **132**, 425-430 (2015).
- 547 52. Zhong Y, Zhou M, Huang F, Lin T, Wan D. Effect of graphene aerogel on
548 thermal behavior of phase change materials for thermal management. *Solar*
549 *Energy Materials and Solar Cells* **113**, 195-200 (2013).
- 550 53. Calderon NR, Martinez-Escandell M, Narciso J, Rodriguez-Reinoso FJJotACS.
551 Manufacture of Biomorphic SiC Components with Homogeneous Properties
552 from Sawdust by Reactive Infiltration with Liquid Silicon. *Journal of the*
553 *American Ceramic Society* **93**, 1003-1009 (2010).
- 554 54. Varela-Feria FM, Ramirez-Rico J, Martinez-Fernandez J, Arellano-Lopez ARD,
555 Singh M. Infiltration and Reaction-Formation Mechanism and Microstructural
556 Evolution of Biomorphic SiC Fabricated by Si-Melt Infiltration. *Innovative*
557 *Processing and Synthesis of Ceramics, Glasses and Composites IX:*
558 *Proceedings of the 107th Annual Meeting of The American Ceramic Society,*
559 *Baltimore, Maryland, USA* **177**, 93 (2012).
- 560 55. Gómez-Martín A, Orihuela M, Ramírez-Rico J, Chacartegui R, Martínez-
561 Fernández J. Thermal conductivity of porous biomorphic SiC derived from
562 wood precursors. *Ceramics International* **42**, 16220-16229 (2016).

- 563 56. Jin Z, Wang J, Qian JJRMM, Engineering. Preparation of biomorphic SiC-
564 ceramics by the reactive infiltration of Si into carbon template derived from
565 basswood. *Rare Metal Materials and Engineering* **33**, 1065-1068 (2004).
- 566 57. Kardashev BK, Nefagin AS, Smirnov BI, Arellano-Lopez ARD, Martinez-
567 Fernandez J, Sepulveda RJPotSS. Elastic and inelastic properties of SiC/Si
568 biomorphic composites and biomorphic SiC based on oak and eucalyptus.
569 *Physics of the Solid State* **48**, 1711-1715 (2006).
- 570 58. El-Kady O, Fathy AJM, Design. Effect of SiC particle size on the physical and
571 mechanical properties of extruded Al matrix nanocomposites. *Materials and*
572 *Design* **54**, 348-353 (2014).
- 573 59. Zimmermann JW, Hilmas GE, Fahrenholtz WG, Dinwiddie RB, Porter WD,
574 Wang HJJotACS. Thermophysical properties of ZrB₂ and ZrB₂-SiC ceramics.
575 *Journal of the American Ceramic Society* **91**, 1405-1411 (2008).
- 576 60. Pickering MA, Taylor RL, Keeley JT, Graves GA. Chemically vapor deposited
577 silicon carbide (SiC) for optical applications. *Proceedings of SPIE - The*
578 *International Society for Optical Engineering* **1118**, 2-13 (1989).
- 579 61. Ishii S, Sugavaneshwar RP, Nagao T. Titanium nitride nanoparticles as
580 plasmonic solar heat transducers. *The Journal of Physical Chemistry C* **120**,
581 2343-2348 (2016).
- 582 62. Liu Z, Liu G, Huang Z, Liu X, Fu G. Ultra-broadband perfect solar absorber by
583 an ultra-thin refractory titanium nitride meta-surface. *Solar Energy Materials*
584 *and Solar Cells* **179**, 346-352 (2018).
- 585 63. Venugopal N, Gerasimov V, Ershov A, Karpov S, Polyutov S. Titanium nitride
586 as light trapping plasmonic material in silicon solar cell. *Optical Materials* **72**,
587 397-402 (2017).
- 588 64. Zhao Y, Yu B, Yu G, Li W. Study on the water-heat coupled phenomena in
589 thawing frozen soil around a buried oil pipeline. *Applied thermal engineering*
590 **73**, 1477-1488 (2014).
- 591 65. Wu B, Lao D, Fu R, Su X, Liu H, Jin X. Novel PEG/EP form-stable phase
592 change materials with high thermal conductivity enhanced by 3D ceramics
593 network. *Ceramics International* **46**, 25285-25292 (2020).
- 594 66. Yang J, *et al.* Hybrid network structure of boron nitride and graphene oxide in
595 shape-stabilized composite phase change materials with enhanced thermal
596 conductivity and light-to-electric energy conversion capability. *Solar Energy*
597 *Materials and Solar Cells* **174**, 56-64 (2018).
- 598 67. Li Y, Li J, Deng Y, Guan W, Wang X, Qian T. Preparation of paraffin/porous
599 TiO₂ foams with enhanced thermal conductivity as PCM, by covering the TiO₂
600 surface with a carbon layer. *Applied energy* **171**, 37-45 (2016).
- 601 68. Li M, Wu Z, Tan J. Properties of form-stable paraffin/silicon dioxide/expanded
602 graphite phase change composites prepared by sol-gel method. *Applied energy*
603 **92**, 456-461 (2012).
- 604 69. Su D, Jia Y, Alva G, Tang F, Fang G. Preparation and thermal properties of n-

605 octadecane/stearic acid eutectic mixtures with hexagonal boron nitride as phase
606 change materials for thermal energy storage. *Energy and Buildings* **131**, 35-41
607 (2016).
608 70. Jia X, *et al.* High thermal conductive shape-stabilized phase change materials
609 of polyethylene glycol/boron nitride@ chitosan composites for thermal energy
610 storage. *Composites Part A: Applied Science and Manufacturing* **129**, 105710
611 (2020).
612

613 **Acknowledgments**

614 This work is mainly supported by China National Key Research and Development Plan
615 Project (Nos. 2018YFA0702300) and National Natural Science Foundation of China
616 (No. 51820105010 and 52076106).

617

618 **Author contributions.**

619 Y.M. conceived the initial idea. X.L. designed the experiments and worked together
620 with Q.X. to complete most experiments. Q.X also wrote the first draft, and X.L. revised
621 it. Y.N and H.L. provided guidance for thermal conductivity and spectral absorption
622 performance testing. M.C helped with the recording and sorting of experimental data.
623 Y.L. and Y.L. tracked the progress of the experiment and revised the manuscript.

624

625 **Competing interests**

626 The authors declare no competing financial interests.

627

628 **Materials & Correspondence**

629 Correspondence and requests for materials should be addressed to X.L.(email:

630 xliu@nuaa.edu.cn) or to Q.X. (email: xuqiao@nuaa.edu.cn)

631

Figures

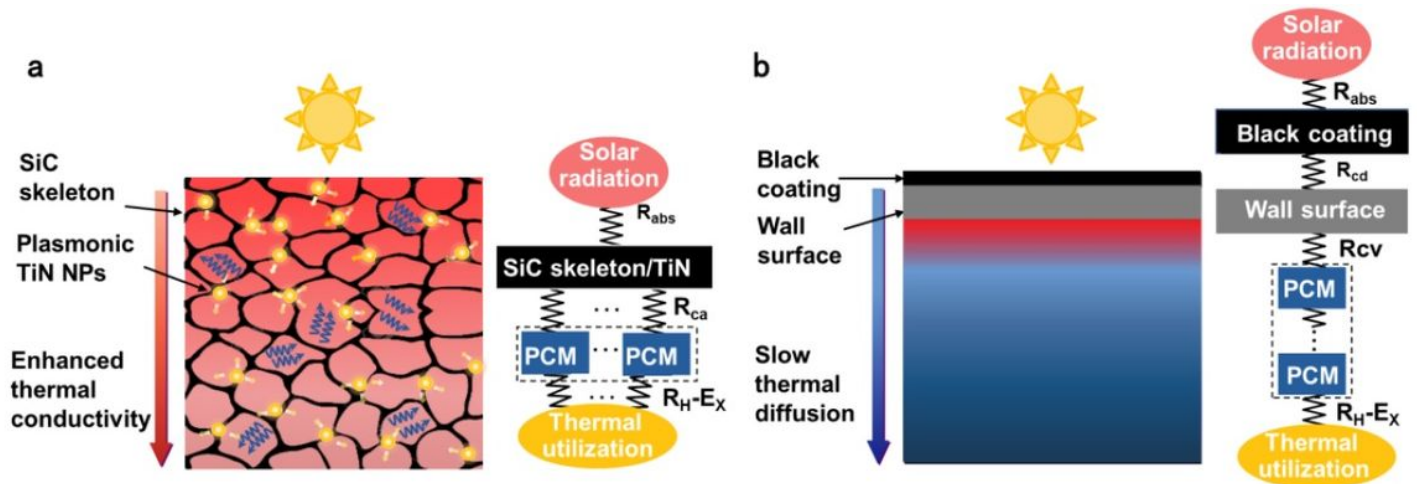


Figure 1

Schematic illustration of solar energy storage. a Integrated solar thermal conversion and energy storage. b Conventional surface-type.

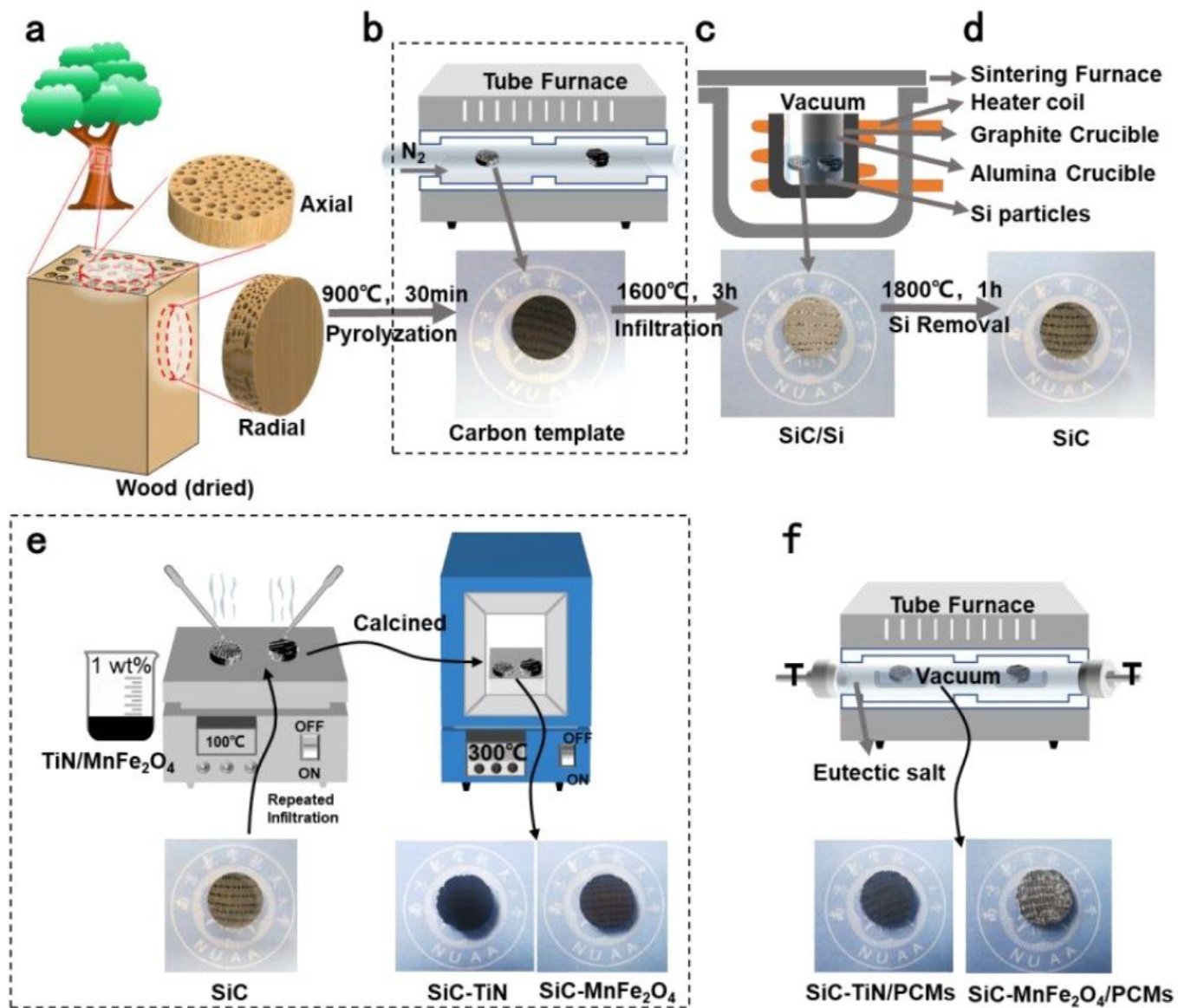


Figure 2

Fabrication processes of nanoparticles decorated biomorphic SiC-PCMs composites.

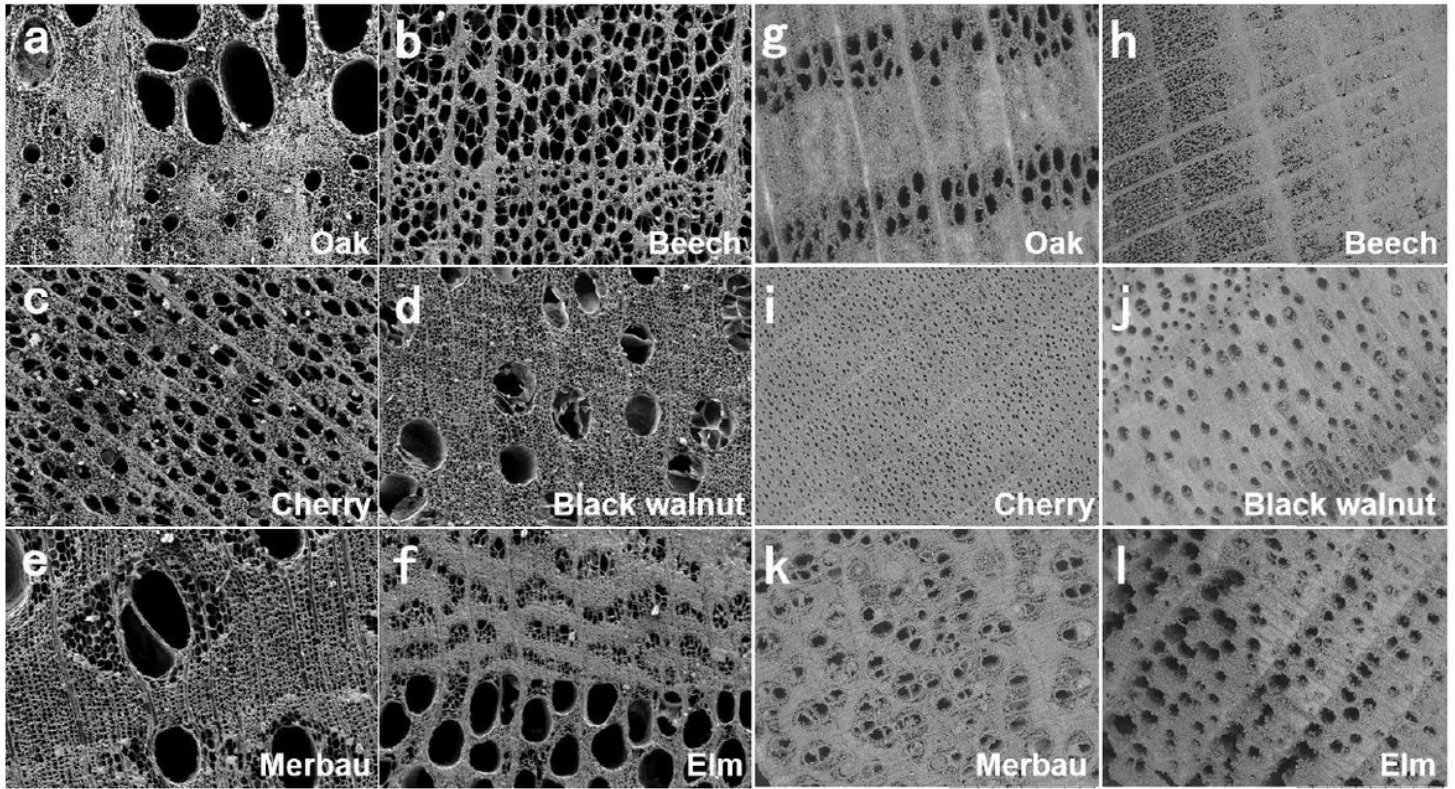


Figure 3

a-f SEM images of carbonized templates (axial sections). g-l SEM images of porous biomorphic SiC ceramics (axial sections).

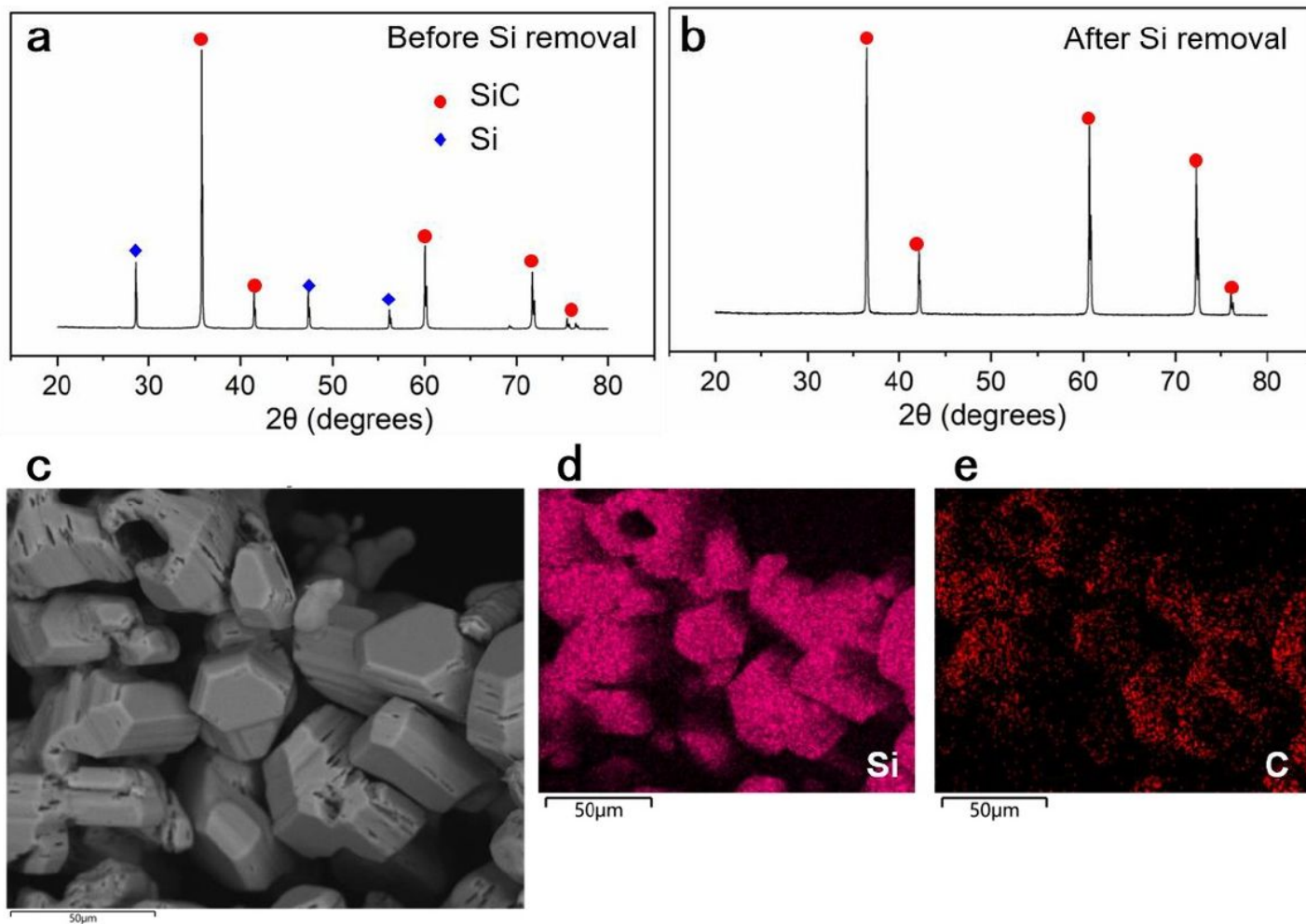


Figure 4

X-ray diffraction patterns of biomorphic SiC ceramics, a before and b after Si removal. c SEM elemental mapping images of biomorphic SiC ceramics, element of d silicon (Si), and e Carbon (C). The ceramic replica was imaged under high vacuum without metal sputtering.

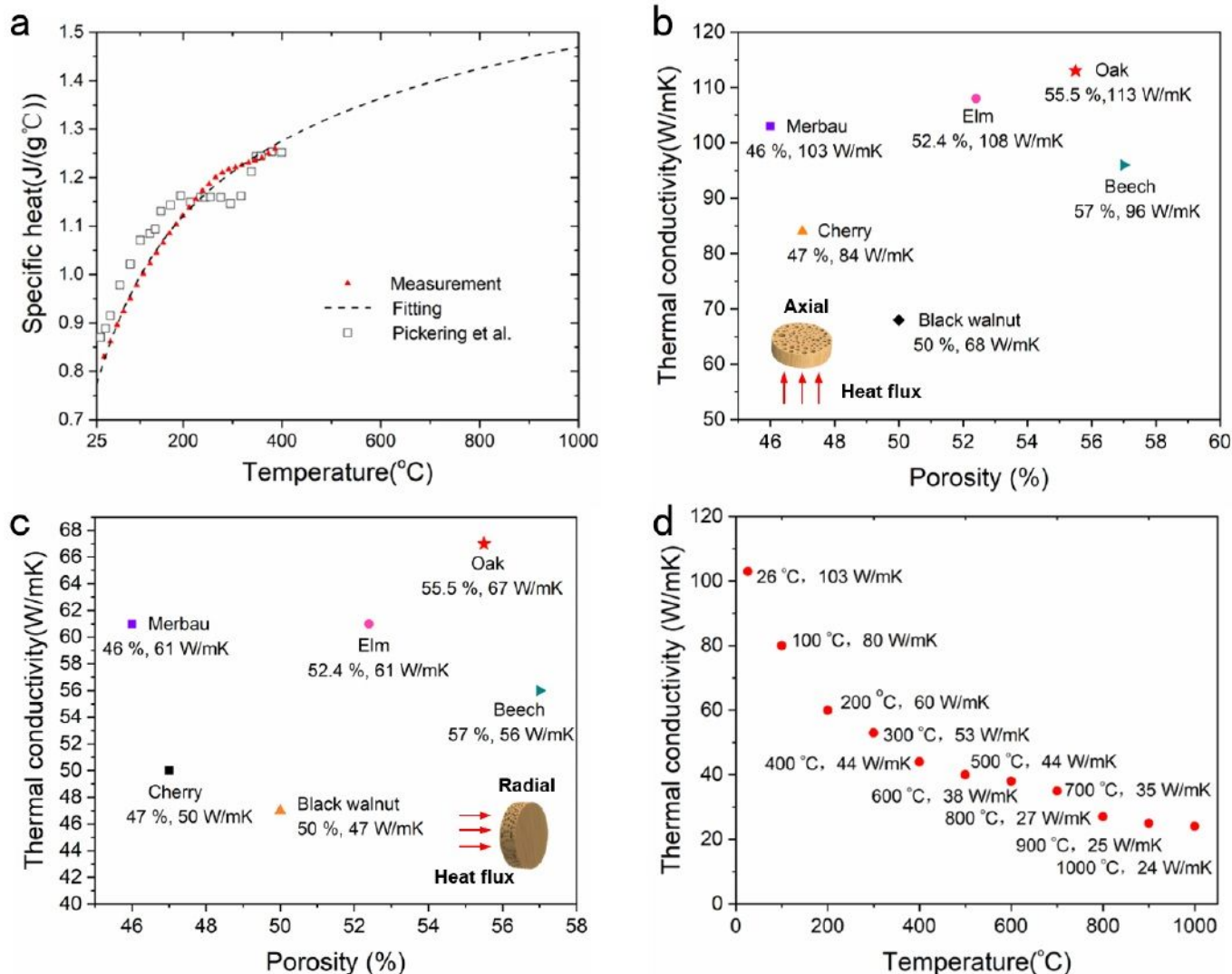


Figure 5

a Specific heat of biomorphic SiC at different temperatures. Thermal conductivity versus porosity at room temperature for both b axial and c radial orientation for six kinds of wood derived SiC ceramics. d Thermal conductivity of Merbau derived SiC at different temperatures in axial orientations.

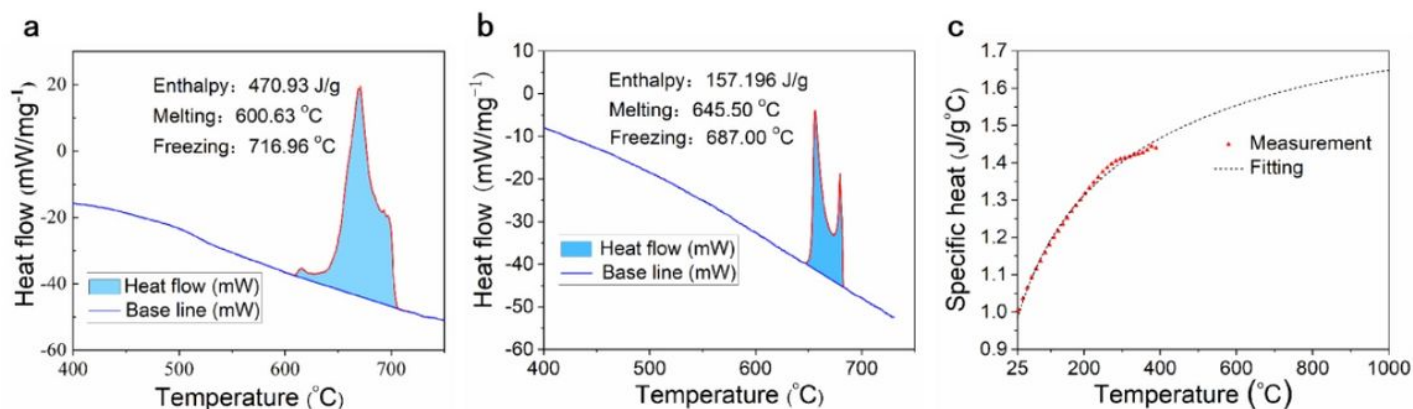


Figure 6

DSC curves of a PCMs, and b SiC/PCMs composites. c Specific heat of SiC/PCMs composites at different temperatures.

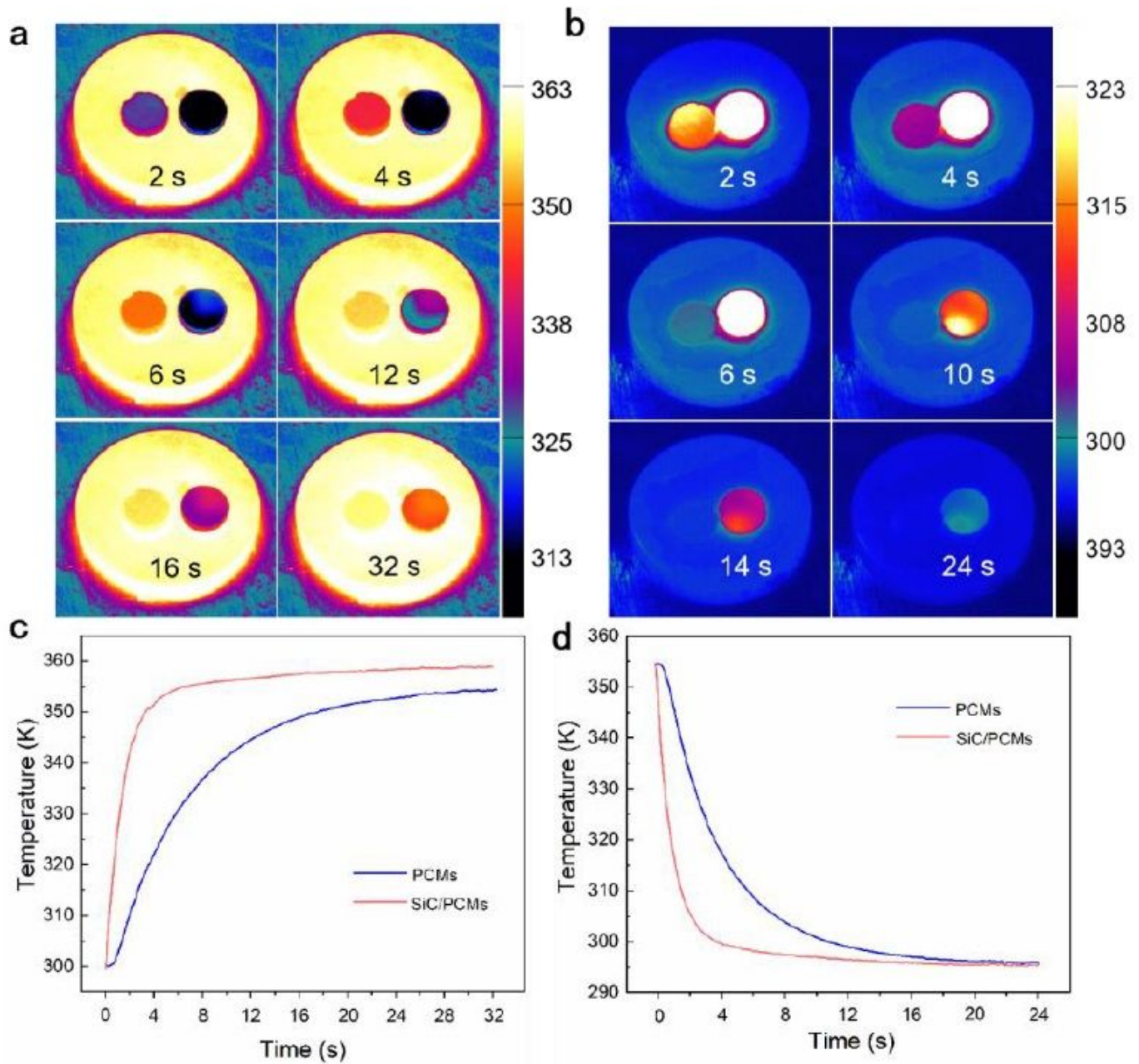


Figure 7

Thermal energy storage properties of SiC/PCMs composites. Infrared thermal images and surface temperature variations for a heating and b cooling processes. Temperature profiles at the center of sample surfaces for c heating and d cooling processes.

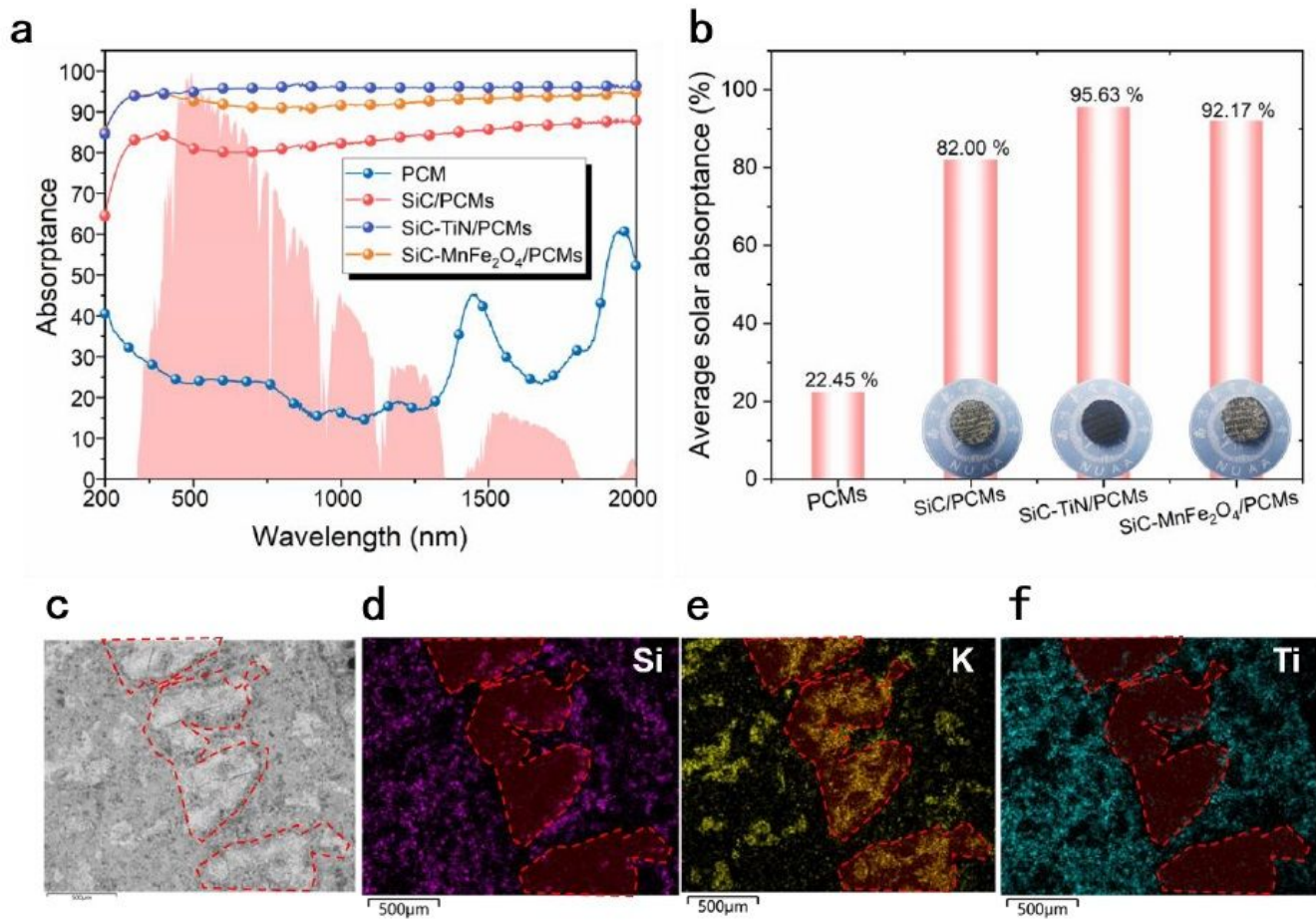


Figure 8

a Spectral and b average solar absorptance of SiC/PCMs, SiC-TiN/PCMs, and SiC- MnFe₂O₄/PCMs. c EDS images of the SiC-TiN/PCMs, elements of d silicon (Si), e potassium (K), and f titanium (Ti).

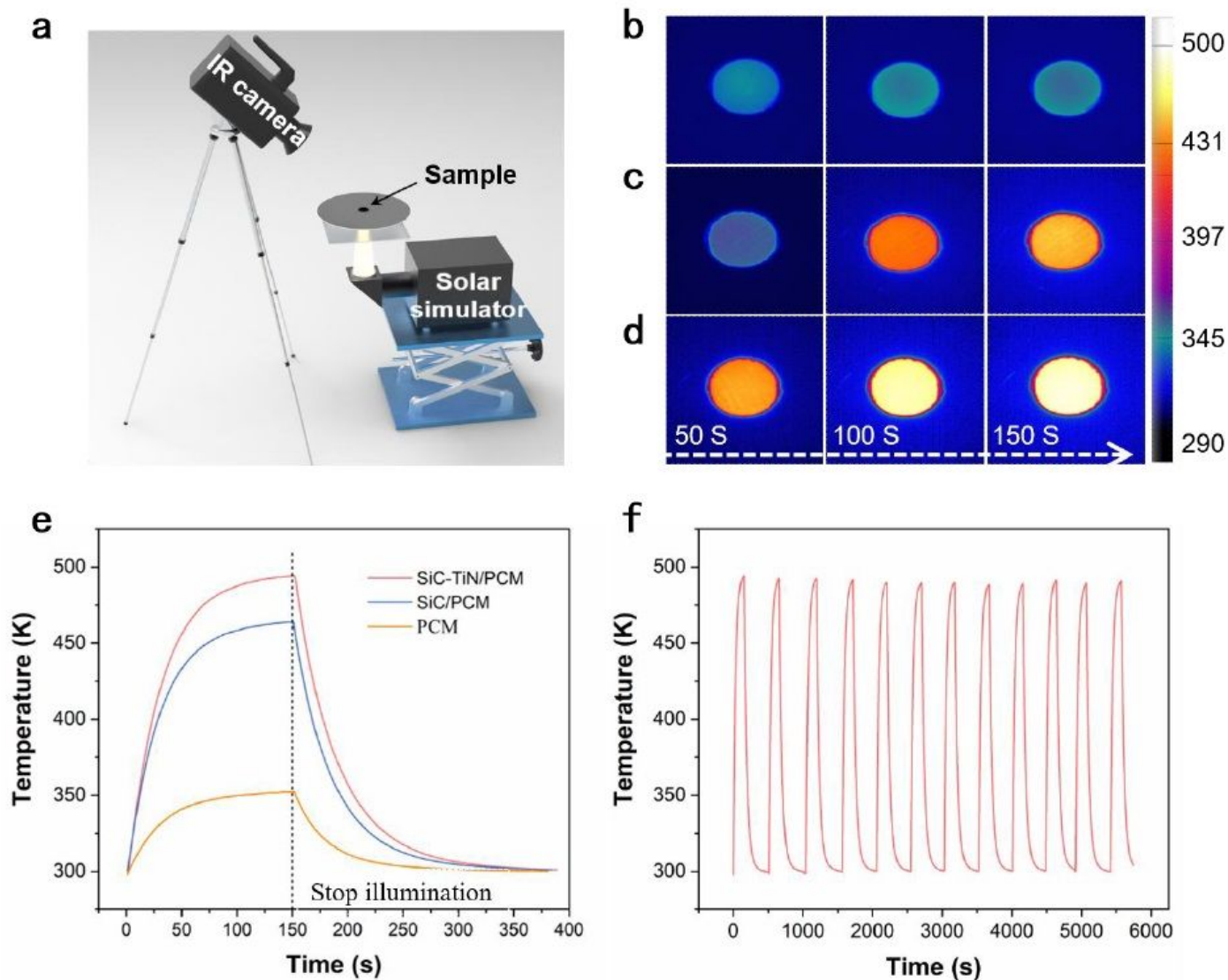


Figure 9

Solar energy storage performances. a Schematic experimental setup. IR images of b pure PCMs, c SiC/PCMs, and d SiC-TiN/PCMs. e Temperature profiles in the center of sample surfaces. f Temperature profiles during repeated heating and cooling processes.

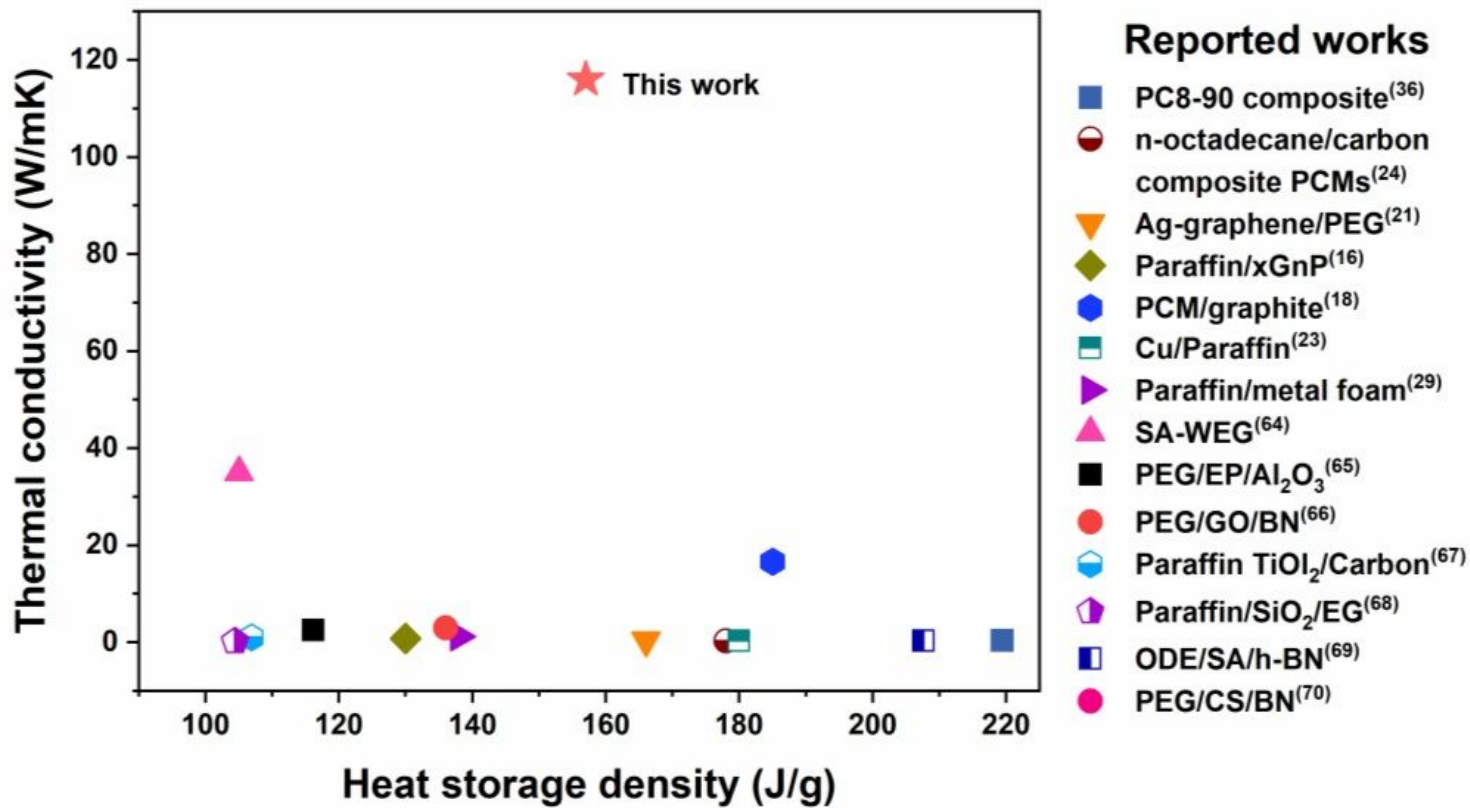


Figure 10

A comparison of the thermal conductivity and heat storage density of phase change composites from the latest reports